POD ANALYSIS OF THE WAKE-BOUNDARY LAYER UNSTEADY INTERACTION IN A LPT BLADE CASCADE

M. Berrino, D. Lengani, D. Simoni, M. Ubaldi, P. Zunino

DIME - Universitá di Genova, Via Montallegro 1, I-16145 Genoa, Italy

ABSTRACT

Particle Image Velocimetry (PIV) measurements have been performed in a low-pressure turbine cascade operating under unsteady inflow conditions to analyze the wake-boundary layer unsteady interaction. Data have been post-processed by means of Proper Orthogonal Decomposition (POD) to improve the understanding of the physics of this complex phenomenon. The method proposed in the paper takes advantage of the POD properties, which consist in splitting spatial (POD modes) and temporal (POD eigenvector) information. The phase identification of each PIV image within the wake passing cycle is extracted from the eigenvectors of properly selected POD modes. The paper describes the procedure employed to sort the experimental PIV snapshots and then reconstruct a phase-averaged velocity field.

A very large data set has been collected to provide phase-averaged distributions of the velocity and turbulence fields with high statistical accuracy. The great spatial resolution of the PIV data allows an in depth analysis of the propagation of the large scale vortical structures recognized at the leading and trailing boundaries of the negative-jet like structure. Furthermore, smaller scale structures embedded within the bulk of the wake have been found to continuously interact with the suction side boundary layer, especially at the leading boundary of the wake where the negative-jet induces local acceleration in the flow.

INTRODUCTION

Boundary layer transition and separation processes along the suction side of Low-Pressure-Turbine (LPT) blades are strongly influenced by the rotor-stator aerodynamic interaction (e.g. Lou and Hourmouziadis 2000; Mailach and Vogeler 2004). Upstream wakes introduce periodic velocity and turbulence fluctuations during their traveling through the blade row, inducing a prompter transition process of the suction side boundary layer as compared with the steady inflow case (Hodson and Howell 2005). Turbulence carried by wakes seems to have an effect on the wake-boundary layer interaction larger than the contribution given by the wake velocity defect (Lou and Hourmouziadis, 2000). In particular, the former is responsible for exciting the boundary layer developing between wakes (Wissink and Rodi 2003; Simoni et al 2013), while the latter generates the so-called negative jet effect (Stieger and Hodson, 2004) that acts transferring momentum toward the wall. These two effects mutually interact with the suction side boundary layer since the apparent jet carries not only momentum toward the wall, but also the smaller scale structures embedded within the bulk of the wake.

Several numerical and experimental studies were carried out in the past to characterize the migration across turbine and compressor rows of unsteady wakes shed from upstream. The DNS of Michelassi et al (2002) and Wu et al (2001) analyzed the dynamics of unsteady wakes that travel from the inlet to the outlet planes of turbine cascades. They were able to recognize the small scale structures embedded within the wake path, as well as to characterize their propagation and interaction with the suction side boundary layer. Similarly, Stieger and Hodson (2005) adopted the laser Doppler velocimeter (LDV) to experimentally characterize the migration of wakes along an highly loaded LPT cascade. This work describes the statistics of turbulence, since LDV is not able to recognize and solve coherent structures embedded within the wake. The authors found large turbulence activity and production rate in the regions where the negative-jet induces, once it impinges on the

wall, the formation of two large scale counter-rotating structures interacting with the blade surface. In particular, a counter-clockwise rotating vortex generates at the leading boundary of the wake patch, while oppositely a clockwise rotating one sets at the trailing boundary of the wake. These vortices are typically referred as Q1 and Q2 vortices, respectively (Gompertz and Bons 2011).

The negative jet has been discussed in great detail in the available literature, but the mechanisms through which the largest scale vortices (Q1 and Q2) carry the smaller scale ones embedded in the wake within the boundary layer is not yet fully understood. To this end, in the present work Proper Orthogonal Decomposition (POD) is applied to a large set of instantaneous PIV snapshots (2000 couples of images), with the aim of recognizing coherent structures within the flow (e.g. Lumley 1967; Legrand et al 2011). The present work focused on the effects induced by both small and large scale structures on the suction side boundary layer transition process during a wake passage period. Phase-locked ensemble averaged velocity, turbulence intensity, and instantaneous perturbation velocity vector maps show that the suction side boundary layer is strongly excited by the smaller scale structures embedded within the wake region only during the former part of the negative jet (during action of Q1). Later, in the region affected by the clockwise large scale Q2 vortex, small scales are not introduced within the boundary layer.

EXPERIMENTAL APPARATUS AND DATA REDUCTION

TEST FACILITY AND INSTRUMENTATION

The experimental investigations have been performed in a blow-down wind tunnel installed at the Aerodynamics and Turbomachinery Laboratory of the University of Genova. The test section is constituted of a 7 blades large scale planar cascade (Fig. 1), representative of highly loaded LPT blade profiles. Blades are characterized by a chord of 120 mm and an aspect ratio AR = 2.5 to ensure two-dimensional flow at midspan. Measurements have been carried out at a low Reynolds number condition Re = 70000. The inlet free-stream turbulence was Tu = 0.19%.

Upstream wakes have been simulated by means of a tangential wheel of radial roads. The wheel rotates in a plane parallel to the cascade leading edges plane. It is located at a distance of 33% of the blade chord upstream of the blade leading edges. The flow coefficient and the reduced frequency were chosen to be representative of real engine operative conditions (φ = 0.675 and f^+ = 0.69). The bar diameter (d = 3 mm) was chosen so that the wakes shed from the bars produce the same losses as those generated by a typical upstream LPT row. The total pressure loss coefficient for the bars was evaluated to be 3.3%.

PIV measurements have been performed in order to characterize the unsteady transition process of the suction side boundary layer perturbed by upstream wakes. The PIV field of view (Fig. 1) covers the flow region $0.74 < s/smax < 1.1$ and $0.0 < y/g < 0.1$. In this region 2000 couples of images have been acquired in order to obtain high statistical accuracy in computing phase-locked quantities, as well as to apply Proper Orthogonal Decomposition (POD).

The PIV instrumentation is constituted by a double-cavity Nd: Yag pulsed laser BLUESKY-QUANTEL CFR200 (energy 2x100 mJ per pulse at 532 nm, pulse duration 8 ns, repetition rate 10 Hz). Since the time-resolution of the present PIV instrumentation is not able to adequately sample the flow evolution in a wake passage period, a technique based on POD mode analysis (Legrand et al, 2011) is applied to sort the instantaneous PIV snapshots in the wake period (see the next section). The optical system forms a light sheet of 1 mm thickness. The light scattered by the seeding particles (mineral oil droplets with a mean diameter of 1.5μm) is recorded on a high sensitive digital camera with a cooled CCD matrix of 1280 x 1024 pixels (with single pixel dimension of 6.7 x 6.7 μm^2). The camera maximum frame rate in the double frame mode is 4.5 Hz, and the minimum frame interval is 200 ns. The magnification factor for the present experiments was set to M = 0.165. The cross-correlation function has been calculated over a 16x16 pixels interrogation area with a 50% overlap. This corresponds to a spatial resolution of 0.325 x 0.325 mm^2. The experimental uncertainty

for the instantaneous velocity has been estimated to be 3.0% of the maximum measurable velocity.

POD FUNDAMENTALS

The Proper Orthogonal Decomposition is nowadays a well established mathematical procedure which has been largely used for the detection of coherent structures embedded within the flow (since Lumley 1967). The POD is performed in the present work following the mathematical procedure described in Sirovich (1987). According to this procedure, given N statistical independent realizations (N PIV instantaneous flow fields), the POD is reduced in finding the eigenvalues Λ and the eigenvectors $\mathbf{X}$ of a cross-correlation matrix $\mathbf{C}$ $[N \times N]$. The i, j element of the matrix $\mathbf{C}$ is defined as the surface integral of the inner product of the vector (or scalar) fields at times i and j. The POD modes are finally obtained projecting the original data on the computed eigenvectors.

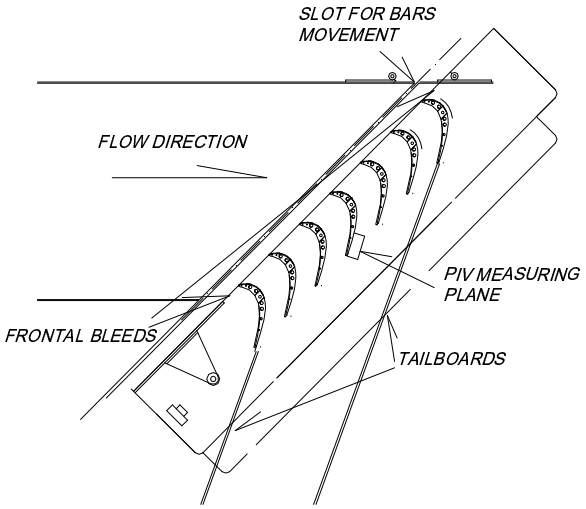

Figure 1: **Sketch of the test section and PIV interrogation area**

These operations can be conveniently expressed and performed in matrix form, since the collected data are discrete in space and time. The set of the N PIV instantaneous flow fields can be collected in a unique matrix $\mathbf{M}$ that has the temporal information (the N images) along the lines and the spatial information (the (x,y) positions) along the columns. In details, each line of $\mathbf{M}$ contains all the data. It is constituted by the velocity components (u,v) for each measurement point (x_i,y_i) for the N PIV instantaneous flow fields, hence $\mathbf{M}$ is defined as follows:

$$\mathbf{M} = \begin{pmatrix} u^{(1)}_{x1,y1} & u^{(1)}_{x2,y1} & \dots & u^{(1)}_{xL,y1} & u^{(1)}_{x1,y2} & \dots & u^{(1)}_{xL,y2} & \dots & u^{(1)}_{xL,yL} & v^{(1)}_{x1,y1} & \dots & \dots & v^{(1)}_{xL,yL} \\ u^{(2)}_{x1,y1} & \dots & \dots & \dots & \dots & \dots & \dots & \dots & \dots & v^{(2)}_{x1,y1} & \dots & \dots & v^{(2)}_{xL,yL} \\ .. & \dots & \dots & \dots & \dots & \dots & \dots & \dots & \dots & \dots & \dots & \dots & \dots \\ u^{(N)}_{x1,y1} & \dots & \dots & u^{(N)}_{xL,y1} & \dots & \dots & \dots & \dots & \dots & v^{(N)}_{x1,y1} & \dots & \dots & v^{(N)}_{xL,yL} \end{pmatrix} \quad (1)$$

where the apex (*) indicates the image number and the terms xL, yL are the number of measurement points along the x and y direction, respectively. Thus, each line of $\mathbf{M}$ has the length of $2 \times xL \times yL$. According to this definition of the matrix $\mathbf{M}$, the cross correlation matrix $\mathbf{C}$ is obtained as:

$$\mathbf{C} = \frac{1}{N}\mathbf{M}\mathbf{M}^T \quad (2)$$

where the surface integral is approximated by the matrix (line per column) product. The eigenvalues Λ and the eigenvectors $\mathbf{X}$ of the cross-correlation matrix $\mathbf{C}$ are obtained solving the eigenvalue problem:

$$\mathbf{C}\mathbf{X} = \Lambda\mathbf{X} \quad (3)$$

Since $\mathbf{C}$ is a symmetric square matrix of size $[N \times N]$, the eigenvalues of $\mathbf{C}$ are then real and non-negative and the eigenvectors are orthogonal (orthonormal according to the solution of the eigenvector problem adopted in the present contribution). The POD modes are computed as:

$$\Phi = \mathbf{M}^T\mathbf{X} \quad (4)$$

This procedure provides a triplet of information: the eigenvalues, the eigenvectors, and the POD modes. The eigenvalue of the i^{th} mode represents the energy contribution of the mode to the total

kinetic energy of velocity fluctuations. The eigenvector of the i^{th} mode retains the temporal information related to each mode (as it will be further discussed in the following). The POD modes constitute an orthogonal basis that provides the spatial information identifying coherent structures in the flow. Hence, the method extracts and separates spatial from temporal information determining the most energetic structures and ordering them by their energy content.

The PIV instrumentation here adopted does not allow a time-resolved acquisition of the phenomena due to the low sampling rate. The properties of POD have been then used to sort the data acquired within the wake passing cycle. Since the POD eigenvectors isolate the purely temporal information, the phase relation of two eigenvectors (typically the first 2 modes) can be used to identify the phase of the individual flow field realization within the wake passage period. Legrand et al (2011) proved that for pseudo periodic convective flows, the eigenvectors of the first two POD modes can be adopted to define a "temporal sorting coefficient" (similar considerations have been empirically obtained by different authors, e.g. van Oudheusden et al 2005). Therefore, the phase ϑ_i of each i^{th} instantaneous velocity field within the cycle of the analyzed periodic phenomenon is determined as:

$$\vartheta_i = arctan(\frac{\chi_i^{(1)}}{\chi_i^{(2)}}) \tag{5}$$

where $\chi_i^{(1)}$ is the eigenvector related to the i^{th} image of the first POD mode (similarly $\chi_i^{(2)}$ to the second one). However, this procedure retains intrinsic ambiguity in the determination of the direction of the flow convection. This is solved forcing the flow convection as the time mean flow direction after phase averaging. The phase averaging procedure is performed with a polynomial fitting (adopting a 11^{th} order polynomial), which solves for each measurement point a least square problem over the 2000 re-ordered images. As discussed in Lengani et al (2014), the polynomial fitting has a statistical error much lower than bin−to−bin averaging.

RESULTS AND DISCUSSION

The time mean boundary layer of the steady state condition shows a large separation bubble that does not reattach before the blade trailing edge. This is depicted on top of Fig. 2 that reports the time-mean streamwise velocity normalized by the free-stream velocity at the measuring domain inlet (U_0). The unsteady inlet condition, with passing wakes through the blade passage, shows a different time-mean boundary layer (bottom of Fig. 2). Indeed, in this latter case the time-mean boundary layer does not present separation. These results confirm the well know beneficial effects of wake blade interaction for highly loaded LP turbine blade profile operating at low Reynolds number (e.g. Hodson and Howell 2005).

The following sections will focus on the detailed analysis of the interaction between both small and large scale coherent structures carried by wakes and the suction side boundary layer. To this end, POD mode distributions will be analyzed to identify the statistical representation of these coherent structures carried by wakes, as well as to sort the instantaneous velocity fields and provide the phase averaged velocity field in the wake passage period.

POD analysis

The eigenvalues Λ are the first information to be analyzed from POD, since they provide the kinetic energy captured by each POD mode. Figure 3 shows the distribution of the POD eigenvalues normalized with the total kinetic energy. POD modes are sorted by energy content, the first mode is the most energetic one and the energy is decreasing for higher order modes. The cumulative contribution of the first 10 modes is about the 45% of the total kinetic energy of velocity fluctuations. The energy of the modes above the 10^{th} becomes rapidly negligible (lower than 1%). This energy distribution suggests that the first modes are associated with large scale coherent structures.

The spatial distributions of the first 2 (most energetic) POD modes are represented in Fig. 3.

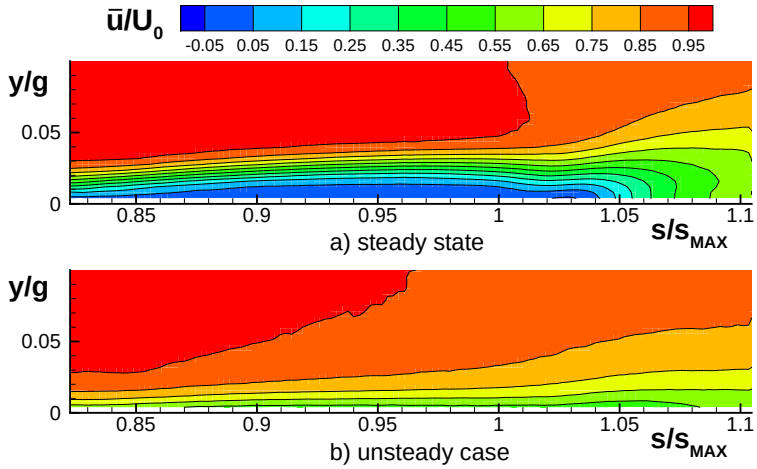

Figure 2: **Time-mean streamwise velocity component, blade to blade plane**

The contour plots represent the POD modes associated with the streamwise velocity component (ϕ_u). The vectorial field superimposed to the contour plot is the vectorial representation of the mode: it is constituted by the components (ϕ_u, ϕ_v) extracted from the POD mode Φ (eq. 4).

The first POD mode shows two distinct regions of the flow at high (positive) and low (negative) values on bottom and top of the investigation area, respectively. The vectorial representation superimposed to the plot shows that the wall normal gradient of ϕ_u is due to a large counter-clockwise rotating vortex. The second mode depicts half of a counter-clockwise rotating vortex in the aft portion of the measurement domain, and a clockwise vortex in the first half. Namely, the first POD mode can be associated to the counter-clockwise vortex, appearing in the perturbation velocity field, formed at the leading boundary of the wake patch when it first impinges on the suction side. The second POD mode resembles the bulk of the so called "negative-jet" structure. It is due to the momentum transfer associated with the wake velocity defect, that generates a 'jet' (visible in the istantaneous phase-locked velocity field) pointing, in the surround of the wake centerline, toward the wall (Stieger and Hodson, 2004). This jet opens in two branches, forming definitively two distinct counter-rotating large scale structures at the leading and trailing boundaries of the wake. Hence, the POD modes clearly identify the dynamics associated with passing wake. Moreover, the first two modes depict similar structures which are spatially shifted by a quarter of their wave length. This is a typical result of POD when pseudo-periodic convective flows are analyzed (Lengani et al, 2014).

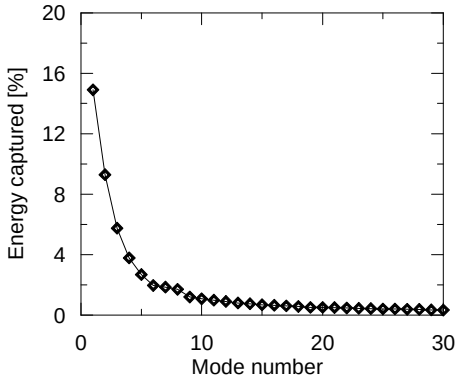

Figure 3: **Relative energy of POD eigenvalues of the u, v kinetic energy**

The pseudo periodic convective flow generated by wake passing events also affects the distribution of the eigenvalues. Figure 5 shows the relation between the values of the eigenvectors of the first two modes. The values on the axes have been normalized. The values of the eigenvectors of the original data are scattered around the center of the plot forming a quasi perfect circle (the fitting of the data is provided as a red continuous curve). The plot differs from the circle just around the point at (x=0.0, y=-1.0), as marked in gray. This discrepancy will be explained in the followings. However, the information provided by the first 2 POD modes and eigenvectors implies that both modes are related to the same pseudo periodic convective phenomenon (e.g. van Oudheusden et al 2005), namely the periodic wake advection along the passage. Thus, equation 5 may be applied to the data set in order to sort the

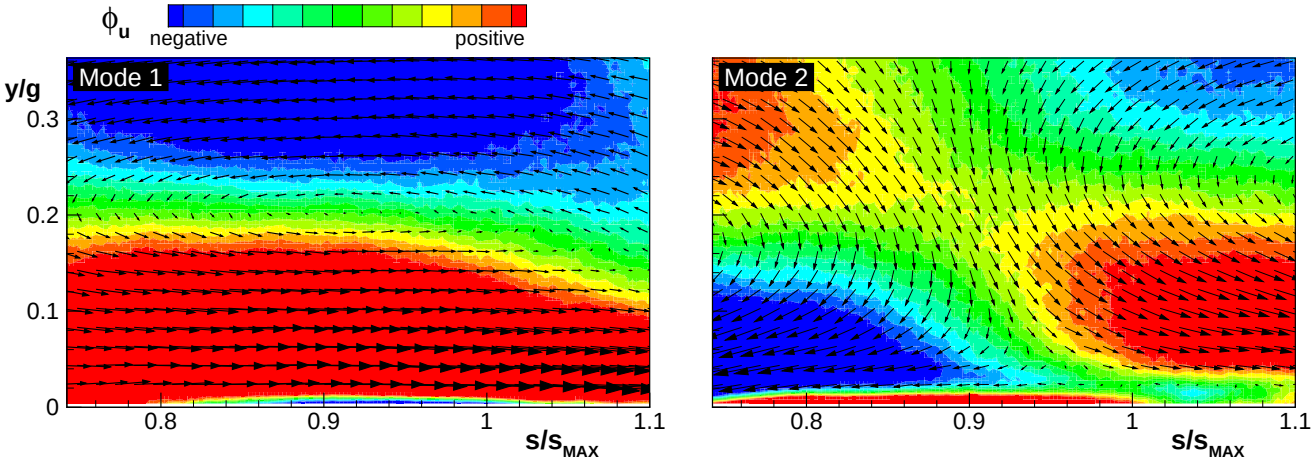

Figure 4: **First two POD modes of the streamwise velocity component and vectorial representation.**

instantaneous images within a wake passing cycle.

As an example of the procedure, Fig. 6 represents 4 re-sorted instantaneous flow fields with the corresponding phase (converted in a non-dimensional time t within the cycle period T). The time mean components of the velocity are removed from the vector fields depicted in the pictures. The first image ($t/T = 0.0$) identifies a flow field with small perturbation velocities. This time instant corresponds to the points at around $(x-axis = 0.0, y-axis = -1.0)$ of Fig. 5. The low intensity perturbations in this image are due to the fact that the previous wake has just leaved the measuring domain, and the successive one is still not entered. It means that at this time instant the istantaneous velocity field itself does not include information on the passing wake structure, periodicity and phase. Thus, the discrepancy from the typical circular distribution in the phase portrait (Fig. 5) can be reasonably attributed to the low influence of the wake passing events around the time instants $t/T = 0.0$.

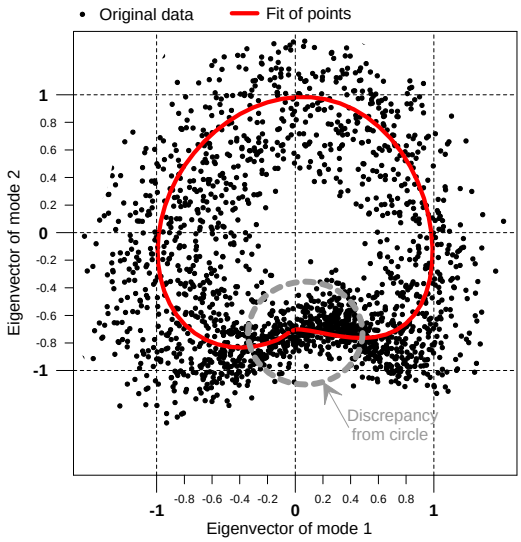

Figure 5: **Phase portrait of the POD eigenvectors, relation between modes 1 and 2.**

The further three images describe the propagation of the incoming wake along the measuring domain. They show much larger value of the perturbation velocity vectors. These effects are related to both the largest scale structures attached to the negative-jet as well as to the smallest scales embedded within the bulk of the wake. To better analyze how these different kind of structures interact with the suction side boundary layer promoting transition, the phase averaged velocity field is described in the next section.

Time-resolved flow field

The phase-averaged experimental data are analyzed according to the triple decomposition of Hussain and Reynolds (1970):

$$u(t) = \bar{u} + < u(t) > + u'(t) \tag{6}$$

where, the term $< u(t) >$ represents the deterministic contribution associated, in this case, with the wake fundamental frequency, and the term $u'(t)$ is the random fluctuation associated mainly with turbulence. The contributions of the time-mean and the purely periodic parts give the phase-averaged velocity $\tilde{u}(t)$:

$$\tilde{u}(t) = \overline{u} + < u(t) > \tag{7}$$

The periodic components $< u >$ and $< v >$ are obtained from this equation as the difference between the phase-averaged velocities ($\tilde{u}$,$\tilde{v}$) and their time-mean values ($\overline{u}$,$\overline{v}$). These velocity components, as well as the instantaneous velocities minus the time-mean values, are referred as perturbation velocities in the following.

The reconstructed phase-averaged velocity field is represented as a plot sequence in Fig. 7. The phase-averaged evolution of the normalized streamwise velocity ($\tilde{u}/U_0$) is depicted as countour plot for the 4 time instants in analysis. The vector maps of the phase-averaged periodic perturbation velocity ($< u >$,$< v >$) are superimposed to the contour plot.

The first instant ($t/T = 0.0$) of the phase-averaged velocity is after the wake has leaved the measurement domain, as previously discussed for the instantaneous re-sorted images. Only the rear part of the clockwise-rotating structures attached to the trailing boundary of the wake can be observed on the top right corner of the measuring domain. This instant shows an attached boundary layer, up to the blade trailing edge ($s/s_{MAX} = 1$), which has higher velocity then the time mean one (note that the perturbation vectors point downstream close to the wall). A further counter-clockwise large scale rotating structure is generated close to the wall (with the eye close to $s/s_{MAX} = 0.9$ and $y/g = 0.07$) that induces local acceleration in the boundary layer region.

The wake enters the measurement domain at $t/T = 0.125$ (not shown). As previously described, the wake-blade surface interaction induces the formation of a negative jet structure which is clearly visible in Fig. 7. At $t/T = 0.5$ a jet pointing toward the wall, that gives rise to two vortices rotating in the opposite direction, can be easily recognized. In particular, the first vortex with counter-clockwise rotation (typically mentioned Q1 in literature, see Gompertz and Bons 2011) is affecting the whole measurement domain for $t/T = 0.25$, strongly accelerating the flow close to the wall. Later, at $t/T = 0.5$ the first vortex is about to leave the field of view while the second (clockwise rotating) vortex attached to the trailing boundary of the wake (Q2) is entering the domain. This clock-wise rotating vortex induces perturbation velocities pointing upstream in the close to the wall region, thus a local thickening of the boundary layer (see the last time instant).

The interaction of the wake with the boundary layer is not limited to the formation of the aforementioned vortices. Indeed, incoming wake-boundary layer interaction generates rollup vortices too, as frequently observed in literature (e.g. Sarkar and Voke 2006; Satta et al 2014). Figure 8 provides a spatial zoom of the time-resolved results of two images acquired at the same phase of the wake period ($t/T = 0.2875$), but acquired at two different passing wake cycles. At this instant, the occurrence of a clockwise rotating vortex with normal to the wall extension of the order of the boundary layer thickness can be observed within the time-resolved boundary layer around $s/s_{MAX} = 0.9$. Instantaneous images acquired for different cycles show that sometimes the flow field is affected by a single vortex (image on the left), while in other cycles multiple vortical structures can be identified (on the right) or they are not identified (not shown in the paper). Results reported in Fig. 7 and Fig. 8 suggest that these vortices originate as a consequence of the strong shear induced by the leading boundary of the wake, where the Q1 vortex contributes to accelerate the flow close to the wall. Anyway, the cycle-to-cycle variation induced by turbulence seems to play an important role too. Indeed, it may be responsible for the different number and structures of rollup vortices observed in the instantaneous images of Fig. 8, which definitively contributes to smear out the visualization of such structures in the phase-locked ensemble-averaged distribution.

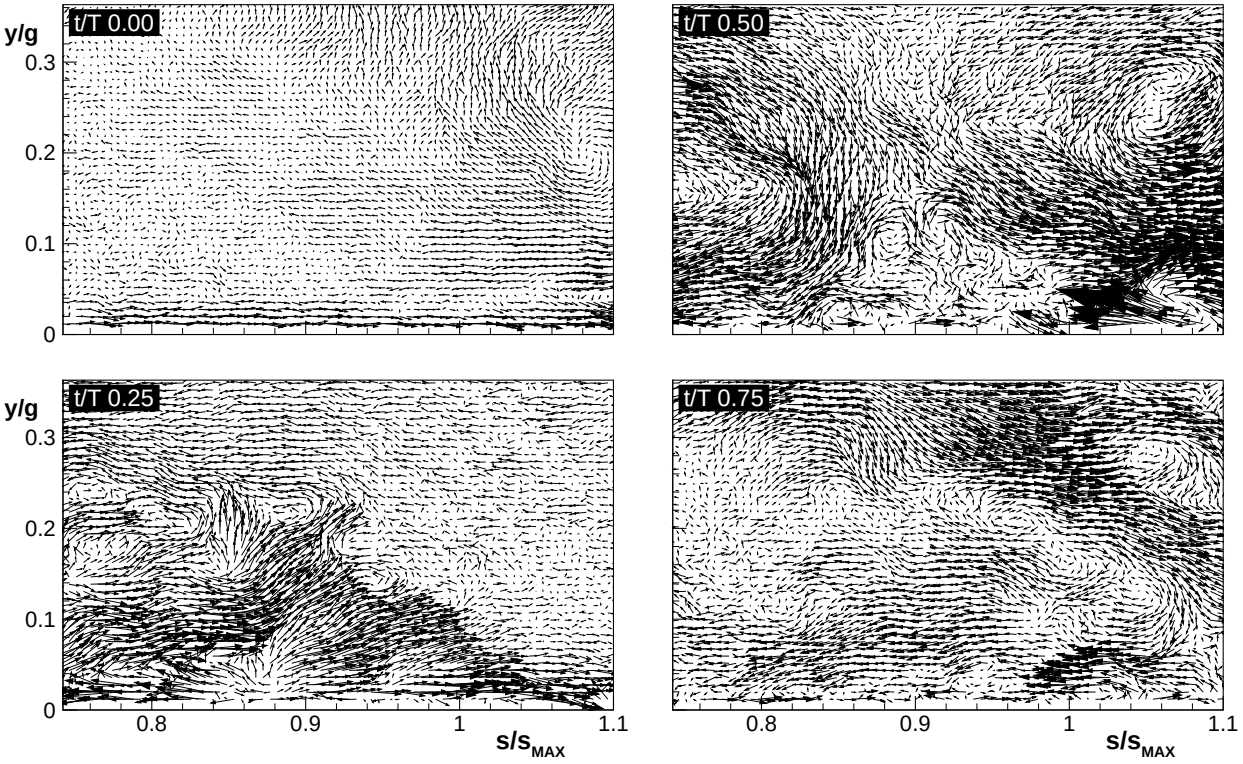

Figure 6: **Instantaneous perturbation velocity vector fields after temporal sorting (see eq. 5)**

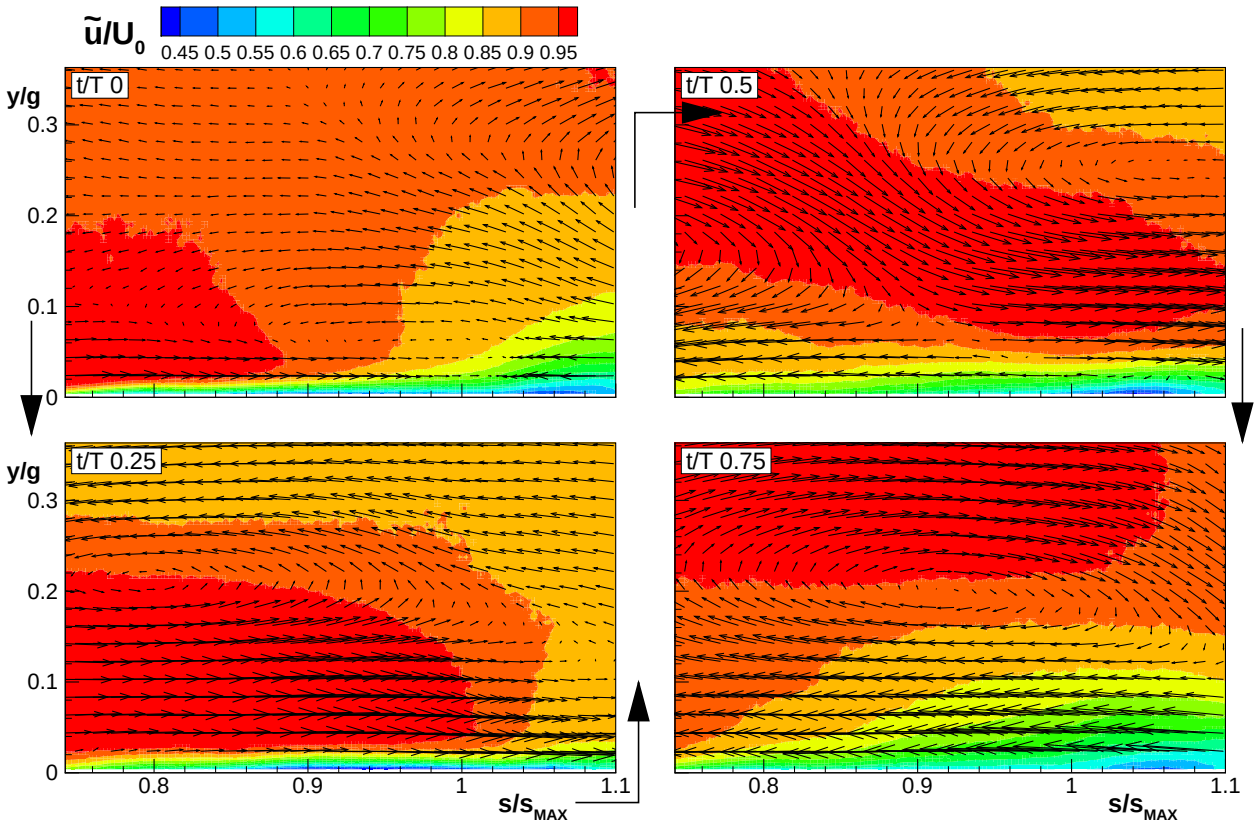

Figure 7: **Time-resolved streamwise velocity and perturbation velocity vector map of the phase-averaged velocity field**

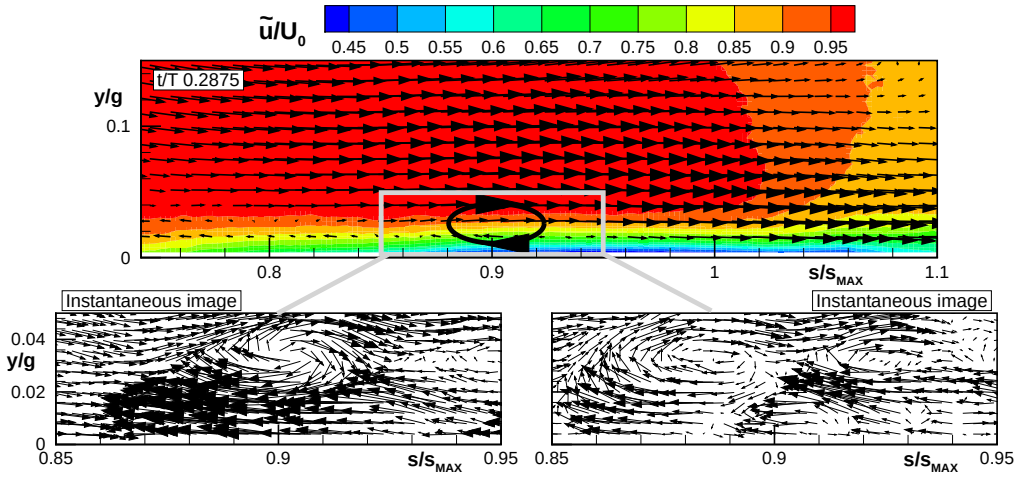

Figure 8: **Zoomed up view of the phase-averaged velocity field (top) and instantaneous perturbation vector maps (bottom) at** $t/T = 0.2875$

Turbulence characteristics

According to the triple decomposition procedure, the acquired data can be further post processed in order to obtain the statistical properties of turbulence. Namely, the root mean square of the stochastic streamwise velocity component ($\tilde{u'}_{RMS}$) has been computed applying a polynomial fitting to the function $(u(t) - \tilde{u}(t))^2$, square root is applied to the fitted result. Results are presented in Fig. 9 in non-dimensional form, dividing the $\tilde{u}'_{RMS}$ for the domain inlet streamwise velocity (U_0). The plot represents the 4 time instants depicted in the previous pictures and the perturbation velocity vectors are superimposed to the plots to identify the positions of the largest vortices attached to the leading and trailing boundaries of the wake.

The largest values of the time-resolved turbulence intensity $\tilde{u}'_{RMS}/U_0$ are always observed within the boundary layer ($y/g < 0.05$). The wake passing events cause large portion of the flow field to have high turbulence. Outside the boundary layer high turbulence levels can be observed within the flow region characterized by positive perturbation velocity (vectors pointing downstream). Elevated values are visible in the flow region affected by the Q1 vortex, while the Q2 one presents relatively lower values in agreement with the LDV measurements of Stieger and Hodson (2005). However, these results provide a statistical analysis of the turbulence evolution in the wake passage period, but no information on the smaller scale structures carried by wakes, and how they interact with the suction side boundary layer can be extracted.

To this end, the PIV data together with POD allow a further analysis step. As previously mentioned, the POD modes and the eigenvectors are orthogonal basis. Hence, the equation 4 ($\Phi = \mathbf{M}^T\mathbf{X}$) can be easily inverted. Setting the amplitude of selected POD modes to zero, and inverting this equation, the flow field (represented by the matrix $\mathbf{M}$) can be reconstructed with a limited number of POD modes. Since the most energetic POD modes are related to the wake passing events (e.g., compare modes 1 and 2 of Fig. 4 with the time-resolved results of Fig. 7), only the higher order modes are related to the smaller scales of turbulence. Equation 4 can be then inverted setting the amplitude of the most energetic modes to zero in order to identify the smaller structures embedded within the wake region.

The results of this operation are provided in Fig. 10. The flow field is here represented as perturbation velocity vectors of selected instantaneous images (the same of Fig. 6). The velocity fields have been reconstructed, as previously explained, retaining just selected POD modes. To this end, the energy of modes below 10 as well as the negligible energy of modes above 400 has been set to zero.

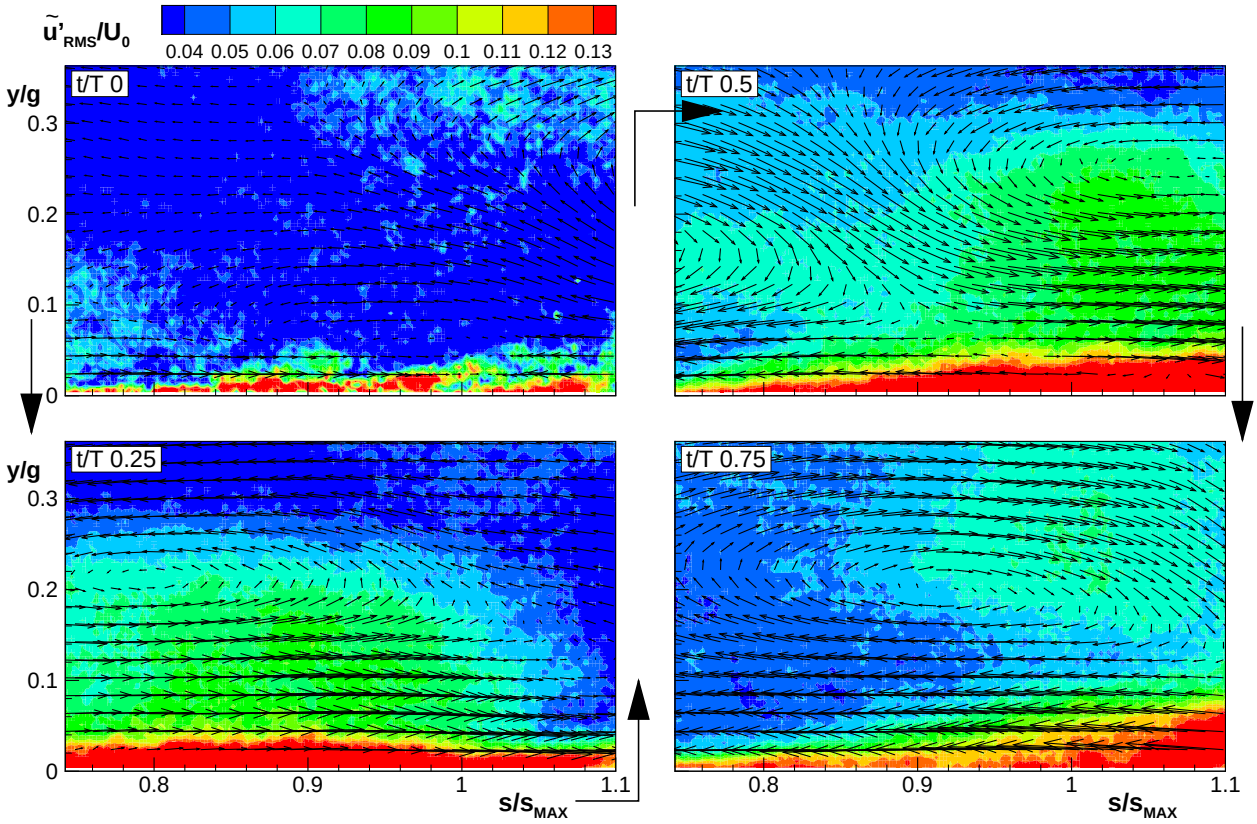

Figure 9: **Root mean square of the stochastic fluctuating streamwise velocity component, phase-averaged perturbation velocity vector maps are superimposed to the plots**

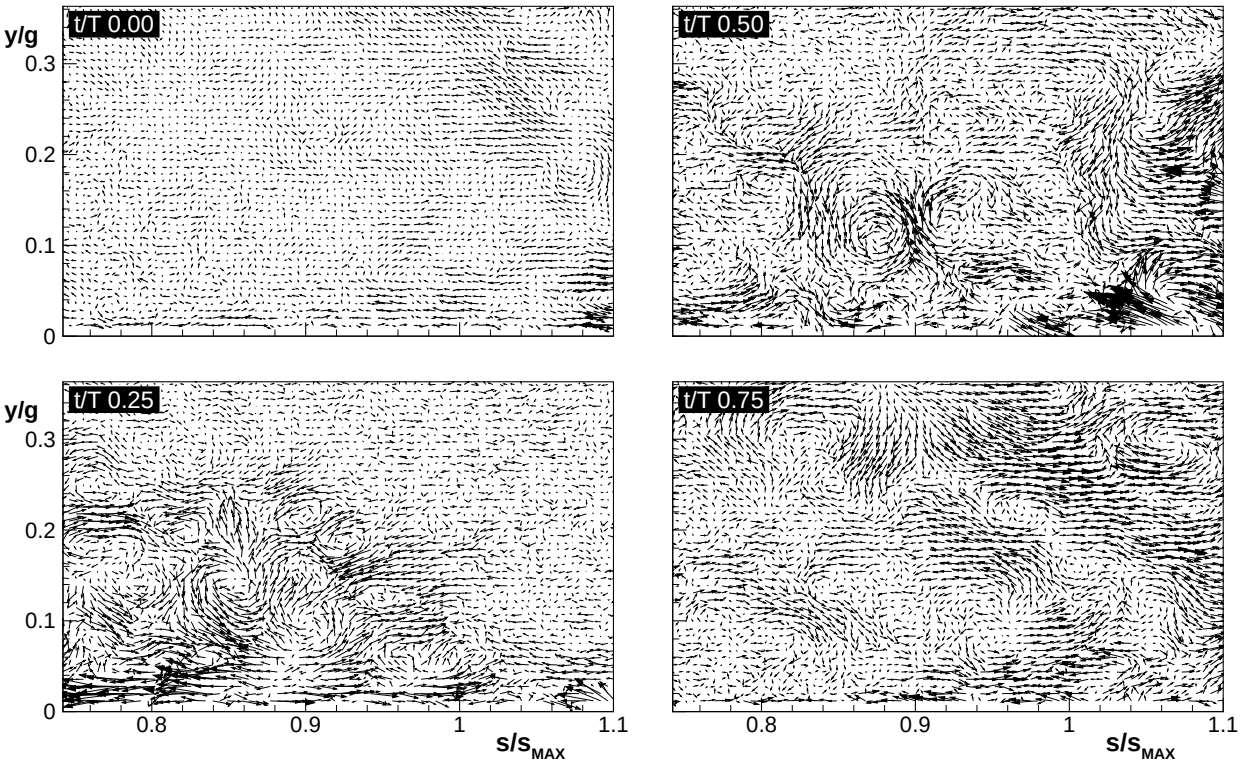

Figure 10: **Instantaneous perturbation velocity vector fields of Fig. 6 which have reconstructed retaining just selected POD modes (10-400) corresponding to 50% of the total energy**

Overall, the energy captured by modes 10-400 is about the half of the total energy. However, the amount of energy captured by the instantaneous images depends on the relative phase of the wake passing event. The perturbation velocity vectors at $t/T = 0.0$ have a very small intensity, since here the wake is just leaving the measuring domain as previously explained. Small scale structures can be identified only downstream of $s/s_{MAX} = 1.0$, where the tail of wake is still present, while the accelerated flow region close to the wall (induced by the counter-clockwise vortex previously mentioned referring to Fig. 7) is not affected by small scales. At this time instant the boundary layer shows the smallest turbulence intensity levels of the whole wake period, since it is not excited by the aforementioned small scale structures. The present results justify the development of a "calmed" unperturbed boundary layer after the wake is passed (Hodson and Howell, 2005). Moreover, no coherent structures are identified in the free-stream without the presence of the wake, probably because their intensity is too small to be correctly captured by PIV.

The correlation between the wake phase and the small scale vortical structures carried by wakes is better appreciated in the further instantaneous images. These images have been selected to highlight the dimensions and structures of the small scale vortical structures carried by wake. The vortical structures embedded within the wake here visualized have the dimension of about the boundary layer thickness ($y/g = 0.05$). They are mainly present in the flow regions affected by the Q1 large scale vortex, especially where it induces acceleration in the flow ($t/T = 0.25$ and $t/T = 0.5$). They are responsible for the high turbulence activity previously observed in Fig. 9. During these phases such small scale structures continuously excite the boundary layer, inducing transition and consequently the high $\tilde{u}'_{RMS}$ levels observed close to the wall in Fig. 9.

Otherwise, at $t/T = 0.75$ small scale structures can be visualized only far away from the wall, where the Q2 vortex again induces positive perturbation velocity. No structures can be observed close to the wall where the perturbation velocity is negative (coherently with the fact that $\tilde{u}'_{RMS}$ has been found low in this flow region in Fig. 9). Thus, the unsteady boundary layer transition seems to be activated by the smaller scale structures carried in the surround of the leading boundary of the wake (where the large scale Q1 vortex acts). Behind the wake centerline small scale structures are no more observed close to the wall, and the boundary layer starts calming, as typically observed in literature (Hodson and Howell, 2005).

CONCLUSIONS

In the present work, POD has been applied to PIV data in order to recognize the effects induced by coherent structures carried by wakes on the unsteady transition process of the suction side boundary layer of a LPT blade. A technique based on the identification of the phase of each PIV snapshot in the wake passage period has been also proved to allow sorting each PIV image in the wake cycle, thus allowing the computation of phase-locked ensemble-averaged distributions.

Inspection of the phase-locked perturbation velocity vector maps shows the large scale clockwise and counter clockwise structures attached to the trailing and the leading boundary of the wake. They have been found to carry the smaller scales embedded in the bulk of the wake within the suction side boundary layer. In particular, the counter-clockwise vortex attached to the leading boundary of the negative jet carries a large amount of small scale structures. These latter are responsible for the high turbulence (statistic) activity observed close to the wall, since they continuously force the boundary layer promoting transition. Moreover, the local acceleration induced by the large scale counter-clockwise vortex in the close to the wall region is responsible for the shear layer rollup, but turbulence carried by wake induces a cycle-to-cycle variation of this phenomenon. Oppositely, in the rear part of the negative-jet where the clockwise structures is attached to the trailing boundary of the wake, small turbulence activity has been observed, since small scale structures are not embedded (and carried) in this wake portion. Thus, the boundary layer can relax in a calmed unperturbed condition after that the bulk of the wake is passed.

REFERENCES

Gompertz KA, Bons JP (2011) Combined unsteady wakes and active flow control on a low-pressure turbine airfoil. AIAA Journal of Propulsion and Power 27:990–1000

Hodson HP, Howell RJ (2005) The role of transition in high-lift low-pressure turbines for aeroengines. Prog in Aerospace Sci 41:419–454

Hussain A, Reynolds W (1970) The mechanics of an organized wave in turbulent shear flow. J Fluid Mech 41:241–258

Legrand M, Nogueira J, Lecuona A (2011) Flow temporal reconstruction from non-time-resolved data part I: mathematic fundamentals. Exp Fluids 51(4):1047–1055

Lengani D, Simoni D, Ubaldi M, Zunino P (2014) POD analysis of the unsteady behavior of a laminar separation bubble. Exp Therm Fluid Sci 58:70–79

Lou W, Hourmouziadis J (2000) Separation bubbles under steady and periodic-unsteady main flow conditions. ASME J of Turbomach 122:634–643

Lumley JL (1967) The structure of inhomogeneous turbulent flows. AM Yaglom, VI Tatarski (Eds), Atmospheric Turbulence and Wave Propagation pp 166–178

Mailach R, Vogeler K (2004) Aerodynamic blade row interaction in an axial compressor part I: Unsteady boundary layer development. ASME J of Turbomach 125:35–44

Michelassi V, Wissink JG, Rodi W (2002) Analysis of DNS and LES of flow in a low-pressure turbine cascade with incoming wakes and comparison with experiments. Flow Turbul and Combust 69:295–329

Sarkar S, Voke P (2006) Large-eddy simulation of unsteady surface pressure overa low-pressure turbine blade due to interactions of passing wakes and inflexional boundary layer. ASME J of Turbomach 128:221–231

Satta F, Simoni D, Ubaldi M, Zunino P, Bertini F (2014) Loading distribution effects on separated flow transition of ultra-high-lift turbine blades. AIAA J of Prop and Power 30:845–856

Simoni D, Ubaldi M, Zunino P (2013) Experimental investigation of the interaction between incoming wakes and instability mechanisms in a laminar separation bubble. Exp Therm Fluid Sci 50:54–60

Sirovich L (1987) Turbulence and the dynamics of coherent structures. part I-III. Q Appl Math 45:561–590

Stieger RD, Hodson H (2004) The transition mechanism of highly loaded low-pressure turbine blades. ASME J of Turbomach 126:536–543

Stieger RD, Hodson HP (2005) The unsteady development of a turbulent wake through a downstream low-pressure turbine blade passage. ASME J of Turbomach 127:388–394

van Oudheusden BW, Scarano F, van Hinsberg NP, Watt DW (2005) Phase-resolved characterization of vortex shedding in the near wake of a square-section cylinder at incidence. Exp Fluids 39:86–98

Wissink WG, Rodi W (2003) DNS of a laminar separation bubble in the presence of oscillating external flow. Flow Turbul and Combust 71:311–331

Wu X, Jacobs R, Hunt JCR, Durbin PA (2001) Evidence of longitudinal vortices evolved from distorted wakes in a turbine passage. J of Fluid Mech 446:199–228